Journal of Applied Physics ARTICLE pubs.aip.org/aip/jap

Investigations of domain wall dynamics in ladder domain wall devices for neuromorphic computing

Cite as: J. Appl. Phys. 138, 093902 (2025); doi: 10.1063/5.0282764
Submitted: 28 May 2025 · Accepted: 4 August 2025 ·
Published Online: 4 September 2025

Hasibur Rahaman, Durgesh Kumar, Ramu Maddu, Bilal Jamshed, Bipul Kumar Mahato, and S. N. Piramanayagam[a)]

AFFILIATIONS

School of Physical and Mathematical Sciences, Nanyang Technological University, 21 Nanyang Link, Singapore 637371, Singapore

[a)]**Author to whom correspondence should be addressed:** prem@ntu.edu.sg

ABSTRACT

Neuromorphic computing (NC) has drawn enormous attention from the research community for its efficacy in artificial intelligence. NC aims to emulate the neurobiological features of neurons and synapses, the building blocks of the human brain. To achieve this, researchers have studied various device designs based on spintronic domain wall (DW) devices. However, there is still a need for more efficient device design with optimized pinning strength. In this paper, we have proposed and studied the concept of ladder DW devices. The device resembles the conventional ladder, and the junction between two consecutive DW segments offers a torque originating from P_{Laplace} on the DW, in a direction opposite to the torque due to the spin–orbit torque. We observed a variety of virtues such as DW pinning, damped DW oscillations, sustained DW oscillations, and DW depinning. Here, the pinned domain walls can effectively mimic the functionalities of neuromorphic synapses. Therefore, we studied the DW motion in ladder devices with eight pinning sites and demonstrated a maximum of 12 multilevel magnetization states, a prerequisite for the synaptic devices. Additionally, the DW oscillations (with a maximum of ∼0.25 GHz frequency) are potentially useful for realizing the neurons. We performed micromagnetic simulations and studied the above-mentioned functions for a wide range of parameters. This study paves the way for new device engineering to achieve multi-functional DW devices, useful for NC. Additionally, two-dimensional DW motion in our devices also opens the possibilities for DW-based logic devices.

I. INTRODUCTION

Artificial intelligence (AI) has significantly improved the quality of life as it can assist us in various areas such as robotics, defense, transport, healthcare, education, banking, chatbots, and gaming.[1,2] Despite the great demand, AI could not reach the desired state-of-the-art because of the enormous energy consumption associated with its hardware. The San Francisco-based AI research lab states that from 1959 to 2012, energy consumption has doubled every 2 years.[3] Presently, AI utilizes machine learning algorithms on the traditional von Neumann computing architecture. Here, the central processing unit (CPU) and memory units are physically separated, which results in a reduction in the operational speed and an enhancement in the energy consumption of the devices.[4,5] Therefore, an alternative computing platform is required. One such alternative architecture is neuromorphic computing (NC), also known as brain-inspired computing architecture, which draws inspiration from a highly energy-efficient and naturally intelligent human brain.[6,7] For instance, the latest supercomputer requires an energy of 10^6 W × h in training a language processing model. However, the human brain can perform all of its activity for over 6 years with an identical amount of energy.[6]

The human brain is a complex network of billions of neurons interconnected through a huge number of synapses. The neurons act as processors, and the synapses act as memory elements. One neuron receives inputs from several other (pre) neurons, and once the input signal reaches a threshold, it fires. Subsequently, the signal is transmitted to the post-neurons via corresponding synapses. The synapse, joining the concerned pre- and post-neuron, controls the signal transmitted between them. The general idea of synthetic NC is building a circuit composed of artificial neurons interconnected through artificial synapses. At the fundamental level, the proximity of neurons and synapses reduces the physical traveling of data between processing and memory units, leading to energy-efficient computations. Like biological counterparts,

multiple synapses can connect the same neurons, with each synapse having a different level of synaptic weight to control the transmitted signal.

Therefore, to achieve the synaptic function, synthetic devices must exhibit multilevel resistance states.[6,8–10] Different methodologies have been developed to fabricate artificial neurons and synapses.[11–13] First approach is to construct electrical circuit using complementary metal–oxide–semiconductor (CMOS) compatible circuit elements.[7] Second possible approach is to employ different functional materials such as ferroelectrics,[14] phase-change materials,[15] spintronics materials,[6,16–23] and resistive materials.[24] The second approach is proposed to be closer to reality as it can enable energy-efficient, compact, and simpler NC architecture. Among the above-mentioned functional materials, spintronic domain wall (DW) devices have been largely investigated due to low energy consumption, high endurance, and non-volatility.[16,25–29] In the beginning, the spin-transfer-torque (STT) was used to drive the DWs. When current is applied through a ferromagnetic (FM) nanowire, the spins carried by spin-polarized current exert a torque on the local magnetic moments of the FM nanowire and thereby induce the DW motion.[30] Later, a spin–orbit torque (SOT) was observed to be more energy-efficient for driving DWs.[31,32] The current density (J) used for DW motion through the SOT is smaller by an order or two, as compared to the STT. When the charge current is passed through a heavy metal (HM) layer adjacent to an FM layer, the bulk spin Hall effect (SHE) and/or interfacial Rashba–Edelstein effect converts the charge current to spin current. This spin current can be used to exert a torque on the local magnetization of the FM and hence drive the DWs. In 2018, Sengupta *et al.* simulated energy-efficient neuromorphic elements in a DW-based magnetic tunnel junction (MTJ) device using the virtues of the SOT.[33,34] Despite growing interest, the field of DW-MTJ-based NC is still in its early phase, with much progress yet to be made toward realizing its full potential.

In MTJ-based spintronic synapses, the reference layer has a fixed magnetization, while a DW in the free layer controls the device resistance to encode synaptic weight. Relying on natural material defects for DW pinning causes variability and reduces control accuracy. To achieve precise and consistent DW positioning across large arrays of MTJs, artificial pinning sites must be intentionally engineered during fabrication.

Researchers have proposed the concept of artificial pinning sites via altering geometric/magnetic properties locally, to realize deterministic multi-resistance (multilevel magnetization) states.[9,35] Initially, researchers used triangular notches to pin the DWs.[36] Kläui *et al.*, studied the triangular notches in ring-like NiFe nanowires and demonstrated the pinning of the DWs.[37] Later, Hayashi *et al.* investigated triangular notches in straight NiFe nanowires and showed successful pinning of the DWs.[38] Parkin *et al.* fabricated multiple triangular notches in NiFe nanowires and observed the successive pinning and depinning of DWs at all the pinning sites.[39] Alternatively, Al Bahri *et al.* proposed the idea of the staggered nanowire to pin the DWs.[40] They performed micromagnetic simulations as well as experiments to observe DW pinning in NiFe nanowires. Kumar *et al.*, have studied meander DW devices, using the Kerr microscopy technique, in W/CoFeB/MgO stack to pin the DW.[16] They also measured anomalous Hall resistance and showed a total of nine multiple resistance states in such devices. More recently, Rahaman *et al.* have utilized the concept of pine-tree DW devices for synaptic applications. They achieved a total of nine multilevel magnetization states.[16,41]

In addition to geometrical pinning methods, several non-geometrical methods were also investigated. Polenciuc *et al.* used exchange bias to achieve the DW pinning.[42] Jin *et al.* studied the ion-implantation B^+ ions, non-magnetic metal diffusion in FM wire, and exchange coupling between out-of-plane magnetized wire (DW device) and crossbars with in-plane magnetization to fabricate the synthetic pinning sites.[8,43] Durner *et al.* used localized stray fields generated by a nanoscopic magnetic inhibitor to pin the DW in a magnetic nanowire.[44] Few groups have explored dipolar interactions between DWs, which were employed to achieve DW pinning.[45,46] Kumar *et al.* have introduced the interfacial Dzyaloshinskii–Moriya interaction (*i*DMI) locally at nanoscale regions to achieve multilevel magnetization states.[47] In addition, the pinning sites have also been suggested to generate oscillating voltages at microwave frequencies in the DW devices via DW oscillations. Sbiaa *et al.* have used stepped nanowires to demonstrate DW oscillation in the GHz frequencies.[48] Voto *et al.* have utilized the geometrical constriction of the shape of double-sided notches in perpendicularly magnetized nanowires to excite spin waves at GHz frequencies.[49] Between geometrical and non-geometrical means, the geometrical pinning sites are more industry-friendly, and therefore, they may be preferred in applications. Despite several geometrical pinning strategies, there is a need for more efficient, fabrication-friendly approaches to achieve optimized pinning strength. Too weak pinning leads to unstable DW motion, while overly strong pinning increases depinning thresholds and power consumption, compromising synaptic weight control. Moreover, in most studies, the number of intermediate magnetization states is limited by the number of pinning sites along the one-dimensional device track. Therefore, increasing pinning sites and intermediate states is essential for enhanced device performance.

In this paper, we have proposed and studied a unique concept of ladder DW devices for NC applications. In such devices, the neighboring DW device segments adjoin at an angle of "θ." When the DW reaches the junctions of two DW device segments, it experiences a geometrical opening. Consequently, it experiences a torque due to the Laplace pressure (P_{Laplace}) on the elastic DW. Due to the competition of torque due to P_{Laplace} and SOT, the DW exhibits interesting dynamics in the form of DW pinning, DW oscillations, and DW depinning. We have performed detailed micromagnetic simulations to investigate DW dynamics in our proposed ladder DW devices. We demonstrated a maximum of 12 multilevel magnetization states in the ladder DW devices with eight pinning sites. Additionally, a maximum frequency of ~0.25 GHz was found in DW oscillation around the pinning sites. In addition to high-speed, multilevel synaptic applications for NC, another intriguing aspect of the ladder DW device is its two-dimensional DW motion, which can be advantageous for spin-based logic devices.

II. SIMULATION METHOD

A. Details of micromagnetic properties

To study the SOT-driven DW dynamics in the proposed devices in detail, we performed micromagnetic simulations using

Mumax3, based on the extended Landau–Lifshitz–Gilbert (LLG) equation,[50]

$$\frac{d\vec{m}}{dt} = -\gamma_0(\vec{m} \times \vec{H}_{\text{eff}}) + \alpha\left(\vec{m} \times \frac{d\vec{m}}{dt}\right) - \gamma_0\vec{m} \times (\vec{m} \times H_{\text{SHE}}\hat{y}), \tag{1}$$

where $\vec{m}$ is the reduced magnetization, γ_0 is the gyromagnetic ratio, α is the Gilbert damping factor, and $\vec{H}_{\text{eff}}$ is the effective magnetic field in the FM system. The effective field can be written as the sum of the fields corresponding to various energies present in the system, which takes the following form in the present case:

$$H_{\text{eff}} = H_{\text{exchange}} + H_{\text{anisotropy}} + H_{\text{demag}} + H_{\text{DMI}}, \tag{2}$$

where the applied external magnetic field term has been neglected, as no external magnetic field was used in our simulations. In Eq. (1), the first term represents the precession of the magnetization induced by the effective magnetic field and the second term accounts for magnetization damping. The last term, representing the Slonczewski-like torque, where H_{SHE} is the effective SOT field due to SHE.[51] This term is modeled using Slonczewski STT parameters within the Mumax3 simulation framework.[52] The simulation parameters used during the simulations are listed in Table I, and these are typically observed in the experimental research of W/CoFeB/MgO material systems.[16,53,54] The DW was driven through SOT in all the simulations where *i*DMI is used for deterministic and field-free DW motion. Moreover, the DW was inserted at the left end of the device and pushed further using DC/pulse current in all the simulations. It 's important to note that the Laplace force is not externally applied but instead arises from the built-in micromagnetic physics implemented in MuMax3.

B. Details of the device geometry

As schematically shown in Fig. 1(a), the neighboring segments of the ladder DW device meet at an angle of θ (in degrees) with respect to the normal (y axis). When several such segments are connected, the DW device resembles the conventional ladder. Therefore, we call our DW devices "ladder DW devices." First, we simulated the ladder DW devices with one pinning site. To get a detailed understanding of a wide range of tilt angles, we studied the DW dynamics for different θ values of 0°, 30°, and 60°. The length of each segment (l_s) is set at 96 nm, while the width (w_1) is fixed at 32 nm. The segments along the $+y$ axis form a cross-connection with those along the $+x$ axis. The above-mentioned cross-connection is a geometrical opening, and therefore, when the DW reaches the vicinity of this region, it experiences P_{Laplace} on the elastic DW. The torque acts in a direction opposite to the torque due to the driving electrical current (τ_{SOT}). To get a deeper insight into the effect of different geometrical parameters on the P_{Laplace}, we studied the DW motion in four different types of ladder DW devices. For this, we studied different combinations of the length (l_v) and width (w_v) of the vertical segments, the width of the cross section between the first and second segments (w_3), and spacing between the horizontal segments (w_2).

Case 1: To get a clearer understanding of the four studied cases, we have presented a schematic of a reference case (i.e., ladder devices with $\theta = 0°$) [see Fig. 1(b)]. Here, we have also defined the characteristic parameters, described above. Note that these simulations were performed in devices with a single pinning site. In case

TABLE I. Simulation parameters utilized during micromagnetic simulations.

Parameters	Value
Cell size	$1 \times 1 \times 1$ nm^3
Exchange length (l_{ex})	~4.9 nm
Spin Hall angle (θ_{SH})	−0.5
Damping constant (θ)	0.012
Exchange constant (A_{ex})	1.5×10^{-11} J/m
Saturation magnetization (M_s)	1×10^6 A/m
*i*DMI constant (D)	0.5 mJ/m^2
Anisotropy constant (K_u)	1×10^6 J/m^3
Anisotropy direction	(0, 0, 1)

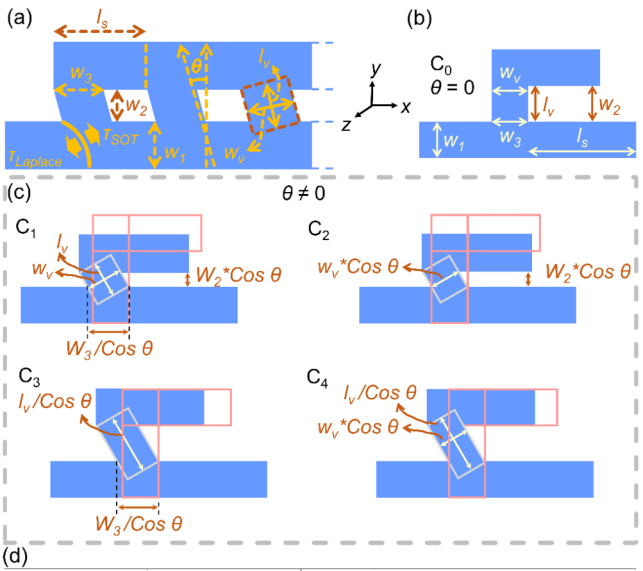

(d)

Cases	w_2 (nm)	w_3 (nm)	w_v (nm)	l_v (nm)	Remarks
C_0	32	32	32	32	C_0-C_4: l_s= 96 nm, w_1= 32 nm
C_1	32*cosθ	32/cosθ	32	32	l_v, w_v, R: same, w_2: ↓, w_3: ↑
C_2	32*cosθ	32	32*cosθ	32	l_v, w_3: same, w_v, w_2: ↓, R: ↑
C_3	32	32/cosθ	32	32/cosθ	w_v, w_2: same, l_v, w_3: ↑, R: ↑
C_4	32	32	32*cosθ	32/cosθ	w_3,w_2: same, l_v, R: ↑, w_v: ↓

FIG. 1. (a) The schematic representation of ladder DW devices. The symbols w_1, w_2, w_3, w_v, l_v, l_s, R, and θ represent the width of the horizontal DW device segment, spacing between the horizontal segments, the cross section between the horizontal and vertical segments, the width of the vertical segment, the length of the vertical segment, the length of the DW device segment, resistance, and the tilt angle of the vertical segment, respectively. (b) The schematic illustration of the ladder devices with zero tilt angle with respect to normal. (c) The depiction of four studied cases, as illustrated below in detail. (d) The table summarizing the variations in parameters involved in the studied cases [corresponding to (b) and (c)].

1, the length and the width of the vertical segment (i.e., l_v and w_v) remain the same for all the studied angles. Consequently, the cross section increases as the angle increases. On the contrary, the spacing between the horizontal segments decreases with the increase in the angle. Here, the magnetostatic interaction between the magnetization in the horizontal segments may come into consideration. Case 1 also implies that the resistance and hence the current distribution in horizontal and vertical segments remains unaffected by the change in the angle. This case is schematically illustrated in Figs. 1(c-C_1).

Case 2: In case 2 [Figs. 1(c-C_2)], the length of the vertical segment (l_v) remains independent of the studied angles. However, the width (w_v) decreases with the increase in the angle "θ." This is to keep the cross section (w_3) constant. These conditions result in the reduction of the spacing between the horizontal DW device segments with the increase in the angle. As the dimensions of the vertical segment change with the change in the angle, the resistance of the vertical segments also carries θ dependence.

***Case* 3:** In case 3 [Figs. 1(c-C_3)], the length of the vertical segment (l_v) increases with an increase in θ. The width (w_v), however, remains the same. This results in an increase in the cross section (w_3), while the spacing between the horizontal segments (w_2) remains the same for all the studied angles. Similar to case 2, the dimension of the vertical segment is angle sensitive, and therefore, the resistance changes with the change in the angle.

***Case* 4:** In case 4, both the length (l_v) and the width (w_v) of the vertical segment change as a function of tilt angle. However, the spacing between the horizontal segments (w_2) and cross section (w_3) remains the same. Moreover, the resistance of the vertical segment changes with a change in θ.

Once we understood the DW dynamics in DW devices with single pinning sites, we extended our simulations for the ladder DW devices with 12 segments. We chose the parameters corresponding to case 1 of the above description. The reason for these choices is discussed in detail in the subsequent sections. Here, the reference device stands for the straight nanowire with the parameters, presented in Table II. As we can see, the distribution of the current density in horizontal and vertical DW device segments plays an important role in SOT-driven DW dynamics in our ladder DW devices. The current density calculation may be trivial in devices with one pinning site. However, it is tricky for the devices with 12 segments. Therefore, to calculate the current distribution in different segments of the DW device, we employed Delta–Wye resistor networks.[55] The details of this scheme are presented in the supplementary material, Sec. 1.

TABLE II. The geometrical parameters of the ladder DW devices with eight pinning sites. Here θ, L, and N represent the angle of tilt of slanted segments, the total length of the devices, and the number of segments, respectively. In addition, w_1, w_2, and w_3 represent the characteristic widths of the design (as described in Fig. 1). LD is used as an acronym for the ladder device.

Device	θ (°)	L (nm)	N	w_1 (nm)	w_2 (nm)	w_3 (nm)
Reference	0	776	1	32		
LD00	0	776	12	32	32	32
LD30	30	660	12	32	28	37
LD60	60	660	12	32	16	64

III. RESULTS AND DISCUSSION

A. Domain wall dynamics in reference domain wall device

To understand and compare the DW dynamics in ladder devices, we first simulated the DW motion in the reference devices (Fig. 2). In the first step, we simulated the DW motion in reference devices at a current density of 5×10^{10} A/m^2 [see Fig. 2(a)]. As can be seen, the DW moves from the left end of the wire to the right without any pinning, which is an expected result. The DW velocity at this current density was found to be 127.6 m/s. Furthermore, we investigated DW motion for a large range of current densities starting from 1×10^{10} A/m^2 to 1×10^{12} A/m^2. However, for the clarity of the plot, we have shown the results for selected current density values (please refer to the supplementary material, Sec. 2 for the rest of the results). These results are presented in Fig. 2(b). Here, the DW position is represented by the z-component of magnetization (m_z). Similar to what was discussed above, the DW sweeps completely from one end of the device to the other for all the current densities. The overall linear variation in m_z with simulation time (t) indicates that the DW moves without pinning in the reference wire. In addition, the slope of m_z vs t increases with the current density, which suggests that the DW velocity increases with the current density.[16,41]

B. Domain wall dynamics in ladder domain wall devices with single pinning site

1. Domain wall pinning

Subsequently, we performed micromagnetic simulations for ladder DW devices with one pinning site (C1–C4 in Fig. 1). The total length of the devices with a single pinning site is 324 nm. To avoid the edge effect due to the demagnetizing energy, we enlarged the extreme segments by a length of 96 nm. For all cases, we inserted DW at a distance of 114 nm away from the left end of the devices. We applied a constant current for 100 ns and observed the SOT-driven DW dynamics. As can be seen in Fig. 3(a), for case 1 and $\theta = 30°$ (current density of 5×10^{10} A/m^2), the DW slowly moved from its initial position toward the pinning site (in about 1 ns), performed damped oscillation for about 15 ns, and got pinned at the pinning site.

To understand the phenomenon of DW pinning, we repeated these simulations for devices with tilt angles of 0°, 30°, and 60° (case 1 for all devices) at current densities ranging from 1×10^{10} A/m^2 to 1×10^{12} A/m^2. DW dynamics results are presented in Figs. 3(b)–3(d). As can be seen, the DW shows the "pinning with damped oscillations" at smaller current densities for all the devices. At intermediate current densities, the DW shows sustained oscillations at GHz frequencies. Upon further increment in the current density, the SOT overcomes the energy barrier, and hence, the DW depins from the pinning site. We defined this current density as the depinning current density (J_{dep}).

From these simulations, we extracted the detailed DW dynamics at the pinning site for a full range of current densities and

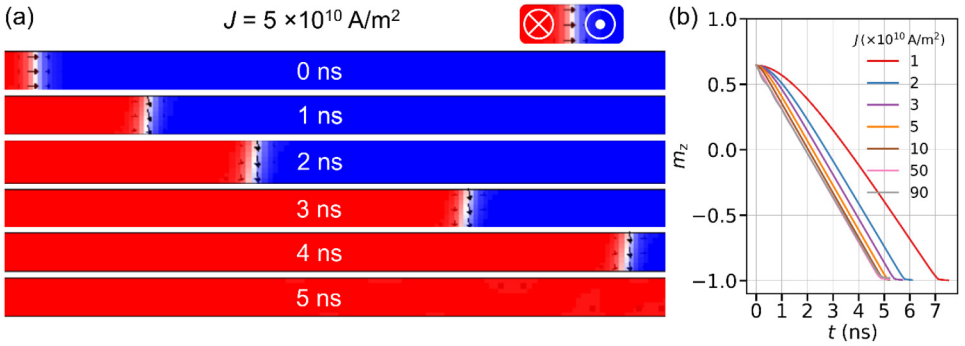

FIG. 2. (a) The simulation snapshots illustrating the instantaneous DW position for the reference nanowire ($J = 5 \times 10^{10}$ A/m^2) at different simulation times. The images have been taken from the initial simulation time ($t = 0$ ns) to $t = 5$ ns in the time interval of 1 ns. (b) The variation in the DW position (m_z) vs simulation time (t) for the reference nanowire at current densities ranging from 1×10^{10} to 1×10^{12} A/m^2. For the sake of clarity, plots corresponding to a few current densities only have been presented.

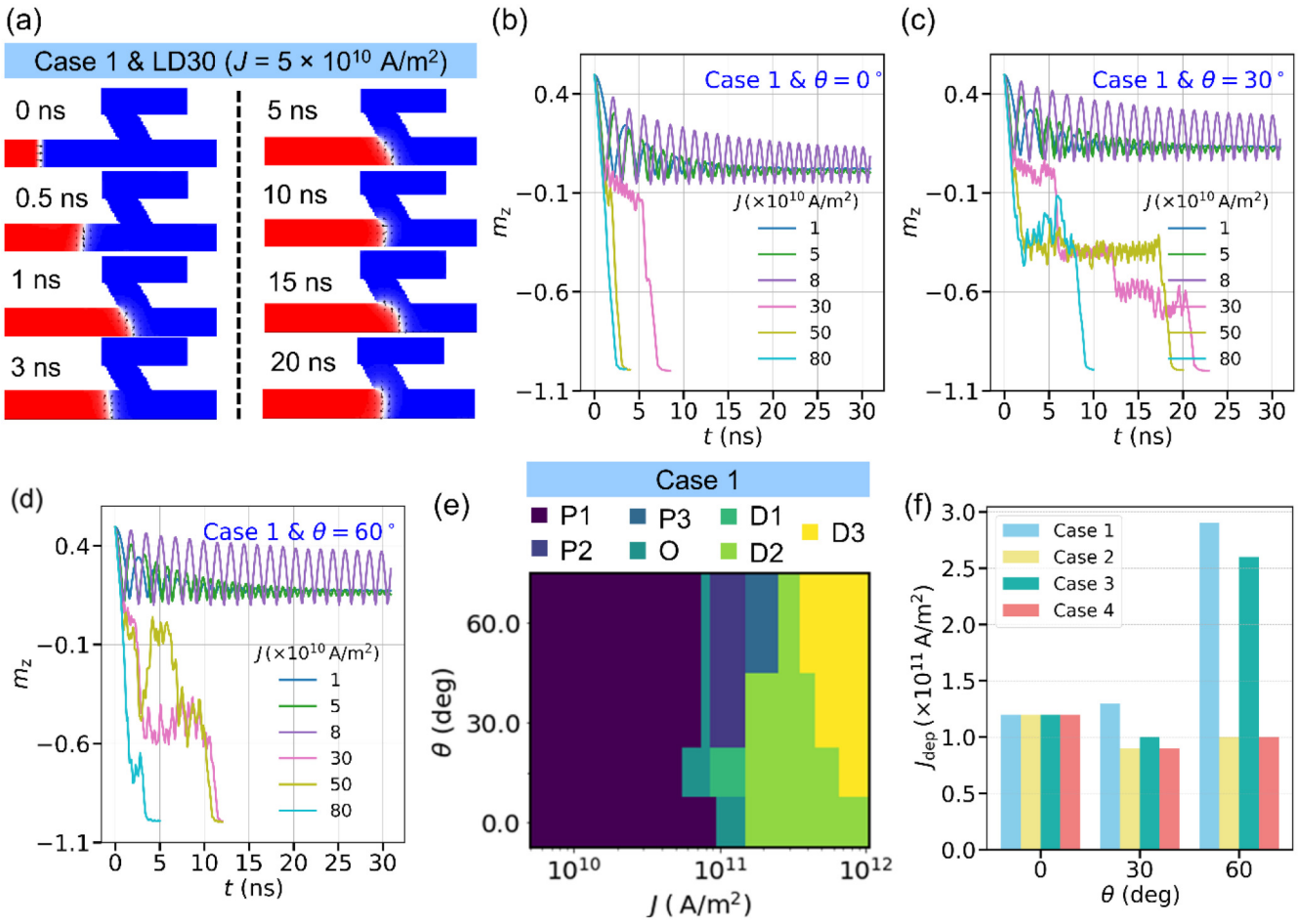

FIG. 3. (a) The snapshots of instantaneous magnetization states in devices with $\theta = 30°$ (case 1) (and single pinning site). The simulation images are taken at different times upon application of $J = 5 \times 10^{10}$ A/m^2. The m_z variation with t at different current densities in devices with (b) $\theta = 0°$, (c) $\theta = 30°$, and (d) $\theta = 60°$ with a single pinning site. (e) The phase diagram of DW dynamics as a function of θ and J. Different names have the following meanings. P1: DW pinning with damped oscillations, P2: DW pinning with distorted damped oscillations, P3: DW pinning with fluctuations. O: sustained oscillations, D1: DW depinning with distorted damped oscillations, D2: depinning, and D3: depinning with nucleation. (f) The variation in depinning current density as a function of θ in different studied cases.

presented them in the phase diagram [see Fig. 3(e)]. The phase diagram comprises a total of seven regions, which are described in the following manner. (i) P1: the region represents the "DW pinning with damped oscillations" at the pinning site. (ii) P2: this region illustrates the "DW pinning with distorted damped oscillations." (iii) P3: in this region, the DW exhibits the "DW pinning with some fluctuations." (*iv*) O: the DW shows "sustained oscillations" in this region. (*v*) D1: in this region, the "DW depins with distorted damped oscillations." And (vi) D2: region and (vii) D3: region show "depinning" and "depinning with random nucleation of domains," respectively. We have included the results for tilt angles 15° in the phase diagram for more details. Please see the supplementary material, Secs. for more discussion on the phase diagram.

Contrary to the DW motion in the reference wire, we observed the pinning of DW for a large range of current densities in all the investigated ladder DW devices. Moreover, the depinning current density increases with the tilt angle for the devices (under case 1). As mentioned earlier, this is because the geometrical expansion at the junctions of segments is the origin of P_{Laplace}, which effectively leads to DW pinning. This P_{Laplace} increases as the tilt angle increases. Since the resistance distribution in the horizontal and vertical segments remains the same for all the devices with different tilt angles, the current distribution plays a minimum role while facilitating the DW pinning at the pinning sites. Generally, in the transition from pinning to depinning events, the DW shows sustained oscillating behavior.

Furthermore, we extended these simulations for the three other cases [see Fig. 1(d)]. The results of case 3 are approximately similar to those we observed for case 1. We summarize these results by presenting the graphs of depinning current density for all the studied cases [see Fig. 3(f)]. This is mainly because the width of the vertical segment remains the same as case 1. Therefore, the torque from P_{Laplace} is expected to be similar. On the contrary, the depinning current density is smaller for both $\theta = 30°$ and $\theta = 60°$ in cases 2 and 4. This is because the width of the vertical segment is smaller for both of these cases. Therefore, the torque due to the P_{Laplace} reduces for both of these cases. In addition, the resistance distribution varies for cases 2, 3, and 4. However, our results indicate that the current distribution may not have a significant effect on the pinning of the DWs in devices with one pinning site. However, this should become critical in ladder devices with eight pinning sites. Our simulation results for all four cases also indicate that cases 1 and 3 are better as compared to cases 2 and 4. Between cases 1 and 3, the resistance distribution is simplistic for case 1. Therefore, we have chosen case 1 for further investigation. Moreover, we investigated the oscillation phenomenon in case 1 in greater detail and we will discuss the results in Subsection III B 2.

2. Domain wall oscillations

If we examine the DW dynamics in greater detail, the bent shape of DW within the pinning site corresponds to a metastable equilibrium, representing a local minimum in the system's total energy. Upon bending, P_{Laplace} is generated, acting as a restoring force that drives the DW back toward its flatter shape. The effect due to P_{Laplace} is the retraction of DW from a pinning site, similar to a ball bouncing off a hard surface. According to the collective coordinate models, DW can behave as a rigid object with effective inertia.[56–58] As a result, DW can retract from the geometrical expansion if the increase in total energy (due to longer DW length) is not compensated by SOT. Rather than immediately settling at the pinning site, the DW dynamics continues to evolve, with magnetic damping gradually dissipating the kinetic energy of DW. When the external driving force is again dominating, it pushes the DW toward the pinning site. This interplay between driving force, restoring P_{Laplace}, inertia, and damping leads to a sustained back-and-forth DW motion, manifesting as DW oscillations.

This oscillatory behavior can be qualitatively modelled with the damped-driven Harmonic oscillator. In the present case, SOT-generated torque acts as a driving force for the DW motion. We first try to comprehend the oscillation dynamics at low $J \ll J_{\text{dep}}$. At this condition, the torque due to P_{Laplace} exceeds SOT. So, in the pinning site we can ignore the effect of applied J. In the absence of J, these oscillations are governed by the balance between the restoring P_{Laplace}, the DW's effective mass and inertia, and damping effects from the magnetic medium.[59] The resulting oscillatory motion is gradually damped out over time as energy is dissipated through magnetic damping.

For small displacements around the pinning site, we can assume that the DW propagates following Newton's second law. This assumption allows us to write a dynamic equation of the damped harmonic oscillator analogous to spring-mass system within a damped medium,

$$m\ddot{x} = -kx - b\dot{x}, \tag{3}$$

where x is the DW displacement from equilibrium and m is the DW mass as defined by Döring.[56] The first term in right-hand side of Eq. (3) represents the restoring force, where k can be interpreted as an elastic constant that depends on the pinning potential (P_{Laplace}). The second term is the intrinsic damping term, where b represents intrinsic damping coefficient proportional to Gilbert damping constant (α) of the material.

The formal solution of the above Eq. (1) is

$$x(t) = e^{-td}\left(C_1 e^{t\sqrt{d^2-w_0^2}} + C_1 e^{t\sqrt{d^2-w_0^2}}\right), \tag{4}$$

where $d = b/2m$ is the damping factor; $\omega_0 = k/\text{m}$ is the natural frequency of the DW in the absence of damping, where k can be interpreted as an elastic constant that depends on the pinning potential (P_{Laplace}); and constants C_1 and C_2 can be determined from the initial boundary conditions. In the underdamped regime, while $d < \omega_0$, Eq. (2) represents the DW dynamics with amplitude gradually decreasing to zero.

From the phase diagram shown in Fig. 3(a), we observed similar findings. As shown in Fig. 3(b), at low $J \ll J_{\text{dep}}$ for the ladder device with $\theta = 0°$, DW undergoes damped harmonic oscillation before being settled (pinning) at the pinning site. This pinning mechanism, followed by damped oscillatory motion, remains consistent across all devices, irrespective of the values of θ.

Besides pinning with damped oscillation, DW also exhibits sustained oscillation, which appears as a transition regime between

pinning and depinning regions. To keep sustained oscillations, the energy lost due to damping must be compensated by SOT. Hence, sustained oscillation begins when the SOT generated by external J becomes comparable to the torque arising from P_{Laplace}. As a result, the system maintains a constant amplitude and frequency of oscillation, with no net increase or decrease in total energy over time. This allows the DW to continuously move back and forth in a kind of resonance condition where maximum DW displacement is observed. The observed sustained oscillations of the DW under constant SOT are indicative of an auto-oscillator regime. The general form for a non-linear auto-oscillator is represented by

$$m\ddot{x} = -kx - b\dot{x} + g(x, \dot{x})\dot{x}. \tag{5}$$

Here, the third additional term represents the non-linear anti-damping (from SOT). The anti-damping term must exceed the intrinsic damping for the onset of self-sustained oscillation as observed in a similar non-linear system such as spin-torque nano-oscillators (STNOs).[60,61]

As discussed earlier, the DW exhibits sustained oscillations over a specific range of current density and magnetic parameters in case 1. As can be seen in Fig. 4(a), when we apply the current with a corresponding current density of 1.1×10^{11} A/m^2 (case 1 and $\theta = 0°$), the DW exhibits sustained oscillations. For a better understanding of the results, we also present a focused view of oscillations (see Fig. S5 in the supplementary material) for the simulation time ranging from $t = 0$ to 5 ns. We have also presented the corresponding instantaneous magnetization states [see Fig. 4(c)]. As we can see, upon the application of the current density with the above-mentioned magnitude, the DW moves toward the pinning site and reaches the pinning site at $t = 1.2$ ns. Here, an additional torque from the P_{Laplace} starts acting on the DW in a direction opposite to the SOT. This torque has dependence on the spatial position as well as time. Under the influence of this torque, the DW travels in the opposite direction. As soon as it reaches a position where the SOT overcomes the torque due to the P_{Laplace} ($t = 2.3$ ns), the DW begins to move forward again. The magnetizations at $t = 1.2$ and $t = 2.3$ ns represent the two extreme positions of the DW during the oscillations. In subsequent times, the DW continues to oscillate between these positions. In all the simulations, we ran the simulations for a simulation time of 100 ns and observed the sustained simulations for the whole time. Oscillatory dynamics in artificial synapses is beneficial as it can enable brain-like temporal processing by bridging synaptic and neuronal functions, allowing a single hardware element or closely integrated module to mimic both synaptic plasticity and neuronal behavior.[62,63] The material parameters

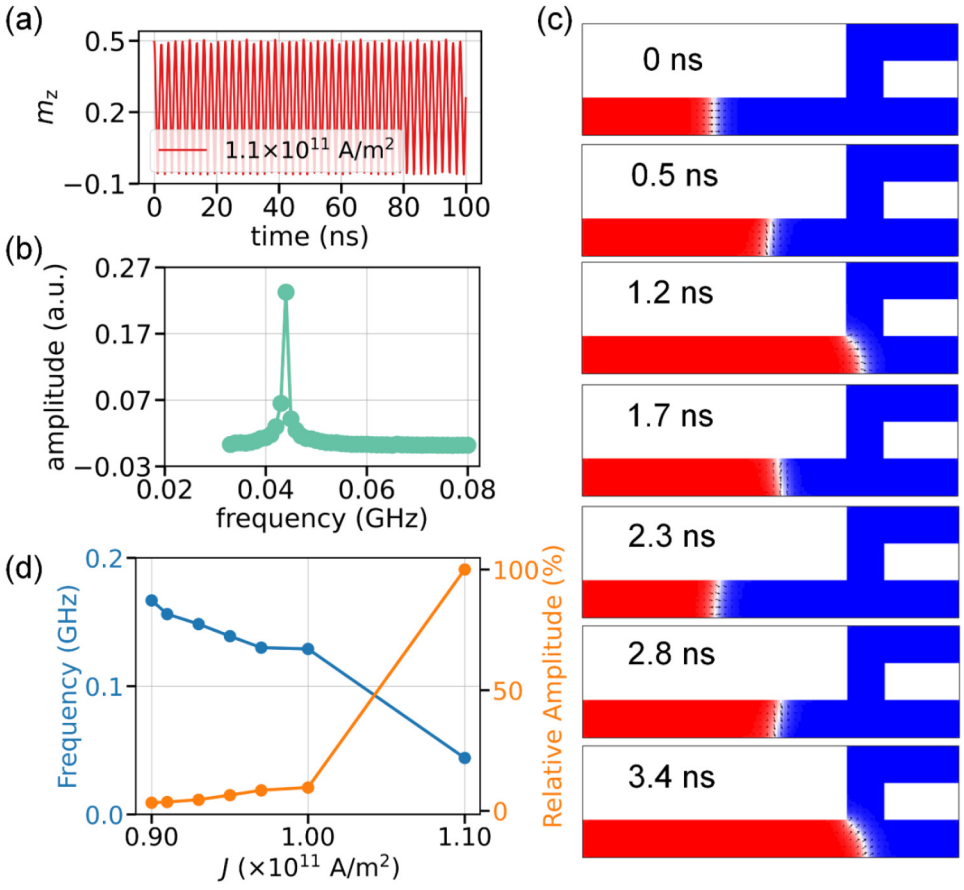

FIG. 4. (a) The DW position (m_z) vs simulation time (t) graph for devices with single pinning site, $\theta = 0°$ (case 1), and $J = 1.1 \times 10^{11}$ A/m^2 (t = 100 ns). (b) Fast Fourier transformation (FFT) of (m_z) vs simulation time (t) plot [presented in Fig. 4(a)]. (c) Depiction of instantaneous magnetization states [corresponding (a)]. The numbers in the images indicate the simulation timescale. (d) The variation in the frequency and relative amplitudes with J for ladder DW devices with $\theta = 0°$.

were also kept the same as listed in Table I of the paper. To estimate the frequency of DW oscillations, we performed a fast Fourier transformation (FFT) of the m_z vs t graph, $\theta = 0°$, and $J = 1.1 \times 10^{11}$ A/m^2. The oscillation frequency was found to be 0.043 GHz [see Fig. 4(b)]. A similar oscillatory behavior of DW dynamics was also observed for ladder DW devices with non-zero θ. These results are presented in Figs. S6(a)–S6(f) in the supplementary material.

In addition, we anticipate that the oscillation frequency and amplitude can be tuned by varying the applied current density. To study this aspect in our simulations, we studied the dependence of the oscillation frequency and amplitude on the applied current density and observed a decreasing trend of frequency and an increasing trend of amplitude with current density in all the devices [see Fig. 4(d)]. A maximum frequency of ∼0.17 GHz was observed in this set of simulations. At smaller current densities, the DWs show some damping in addition to sustained oscillations. As the current density reaches a certain value, a perfect resonance condition is obtained. This is the reason we observed an increasing trend in the amplitude. In addition, when the DW travels a long distance, it should take a longer time to complete one cycle of the oscillations. This is why we see a decreasing trend in the frequency as the current density increases. A further increase in the current density causes the depinning of the DW. This is because the SOT overcomes the energy barrier. We have also presented the simulation results for ladder DW devices with non-zero θ in Figs. S6(h) and S6(i) in the supplementary material.

Subsequently, we also observed that the oscillation frequency and the amplitude are tunable with respect to the magnetic parameters and, therefore, we performed detailed micromagnetic simulations to understand the effect of material parameters like M_s, K_u, and A_{ex} on the DW oscillations. Here, we have discussed the results corresponding to devices with $\theta = 0°$. Similar observations have been obtained in other devices as well. We first fixed the current density at $J = 1.1 \times 10^{11}$ A/m^2 and varied saturation magnetization (M_s). These results are presented in Fig. 5(a). For M_s lower than 0.7×10^6 A/m, DW shows strongly damped oscillations followed by pinning at the first pinning site. As M_s increases, the amplitude of oscillation increases, and the dynamics transit toward sustained oscillation. The maximum amplitude of oscillation corresponds to $M_s = 1 \times 10^6$ A/m, which was previously used for all simulations. For M_s values of 1.1×10^6 A/m and 1.2×10^6 A/m, DW depins and completely sweeps the device. A maximum frequency of ∼0.3 GHz was observed in this set of simulations. This situation is similar to the one we observed in the variation in the frequency and amplitude with current density, and therefore, the oscillation frequency reduces as saturation magnetization increases, which is an expected result. In addition, an increase in M_s causes a decrease in P_{Laplace}.[64] A reduction in the restoring force reduces the oscillation frequency.

Furthermore, we studied the effect of the anisotropy constant (K_u) on DW oscillation [see Fig. 5(b)]. At K_u smaller than 1×10^6 J/m^3, the energy barrier is too low. So, the DW easily crosses the pinning site without any effective pinning. This is because P_{Laplace} is directly proportional to the anisotropy constant of the material.[64–66] The maximum amplitude for sustained oscillation is observed at $K_u = 1 \times 10^6$ J/m^3. Above $K_u = 1.2 \times 10^6$ J/m^3, the DW gets pinned firmly at the pinning site after performing damped oscillations. Moreover, as the anisotropy constant increases, the frequency increases and amplitude decreases. A maximum frequency of ∼0.25 GHz was observed in this set of simulations. The nature of DW oscillation as a function of K_u is opposite to that observed for M_s. This is because saturation magnetization and anisotropy constant have opposite effects on the restoring force. As shown in Fig. 5(c), we have also studied the effect of the exchange constant on the frequency and amplitude of DW oscillations. In the range $A_{ex} = 0.5 \times 10^{-11}$ J/m to $A_{ex} = 1.5 \times 10^{-11}$ J/m, DW dynamics show oscillations. However, it shows a negligible effect on the frequency of oscillations. A maximum amplitude for sustained oscillation is observed at $A_{ex} = 1.5 \times 10^{-11}$ J/m. From $A_{ex} = 1.5 \times 10^{-11}$ J/m to 2×10^{-11} J/m, the DW shows depinning with distorted damped oscillation. A maximum frequency of ∼0.18 GHz was observed in this set of simulations. We have also presented the complementary details of DW oscillations in the supplementary material, Sec. 6.

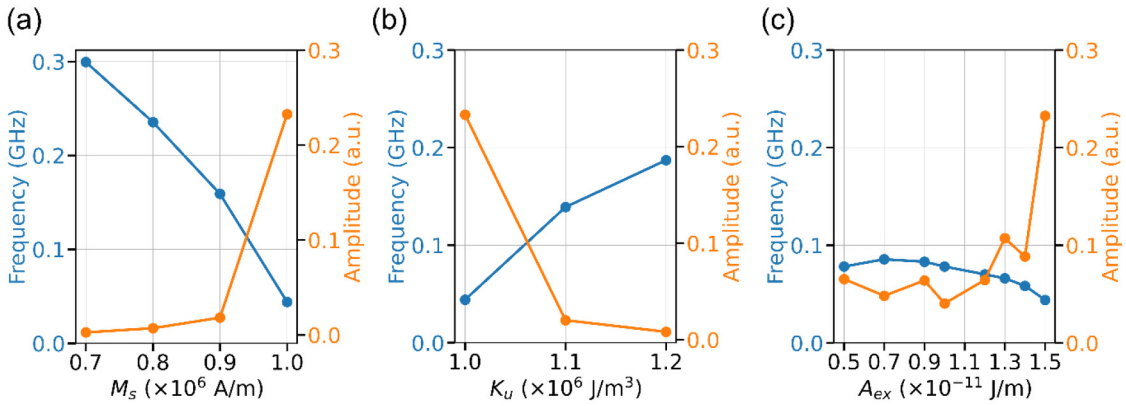

FIG. 5. (a) The variation in the DW oscillation frequency and amplitude with (a) M_s, (b) K_u, and (c) A_{ex} for $\theta = 0°$. Here, $J = 1.1 \times 10^{11}$ A/m^2 was applied for 100 ns.

C. Multilevel magnetization states

Finally, we performed the micromagnetic simulations for the full ladder DW devices—containing 12 segments—to achieve multilevel magnetization states. We considered the ladder DW devices with geometrical parameters corresponding to case 1. Before applying the current pulses to realize multilevel magnetization states, we also applied the DC for the full ladder device and observed approximately similar phase diagram of DW dynamics as we observed for a single pinning site. These results have been presented in the supplementary material, Sec. 7. Subsequently, we applied the current pulses to achieve multilevel magnetization states. The magnitude of the current density was chosen in such a way that the current density is either equivalent to or slightly higher than the depinning current density. Moreover, the pulse widths were optimized to push the DW from one pinning site to the next one. First, we performed these simulations for LD00 and observed a staircase-like variation in the magnetization. A total of six magnetization states were achieved in this case [see Fig. 6(a)]. In these devices, a current density of 6×10^{11} A/m^2 was utilized. One can also see that constant magnetization states are not flat.

The instability in the multi-level states can be attributed to two primary factors. The full ladder DW device hosts multiple DWs. As a result, while one DW is pinned, others may still be moving, causing fluctuations in the multilevel magnetization states. A potential solution is to implement a feedback-controlled calibration mechanism that actively monitors DW positions and finalizes the synaptic weight update only when all DWs are simultaneously pinned. However, integrating such sensors and control circuitry into dense neuromorphic arrays requires careful design to balance complexity, power consumption, and scalability. Future research is needed to optimize system-level integration for large-scale, low-power neuromorphic architectures.

Besides this, inter-DW dipolar interactions also contribute to instability. As discussed before, this effect can be mitigated by optimizing material parameters—for example, reducing the saturation magnetization (M_s) and tuning the effective anisotropy (K_{eff})—to minimize stray fields and thus inter-DW coupling. Additionally, optimizing the spacing between horizontal segments can further reduce dipolar interactions and enhance the stability of intermediate magnetization states.

Furthermore, we repeated these simulations for LD30 [see Figs. 6(b) and 6(d)]. In these devices, we applied a current density with the magnitude of 3×10^{11} A/m^2 and different pulse widths (based on optimized parameters). As can be seen in Fig. 6(d), the DW reaches the first pinning site from the nucleated site in 1.5 ns. Once it reached the first pinning site, we turned off the current and observed the DW dynamics. The DW gets pinned at the first pinning site. As mentioned earlier, the geometrical expansion at the pinning site hosts the DWs in the current off-period. We further applied the same current density, and, as a result, the DW leaves the first pinning site and moves further. This process continues, and a total of 12 magnetization states were observed for LD30 devices. Finally, we performed similar simulations with the LD60 devices, and a total of 7 magnetization states were observed [see Fig. 6(c)]. A current density of 3×10^{11} A/m^2 was utilized in these devices as well. The reason for the reduction in the magnetization states is the increased pinning strength of the pinning sites. In this situation, controlling the pinning and depinning process becomes difficult. In addition, larger pinning strength causes the nucleation

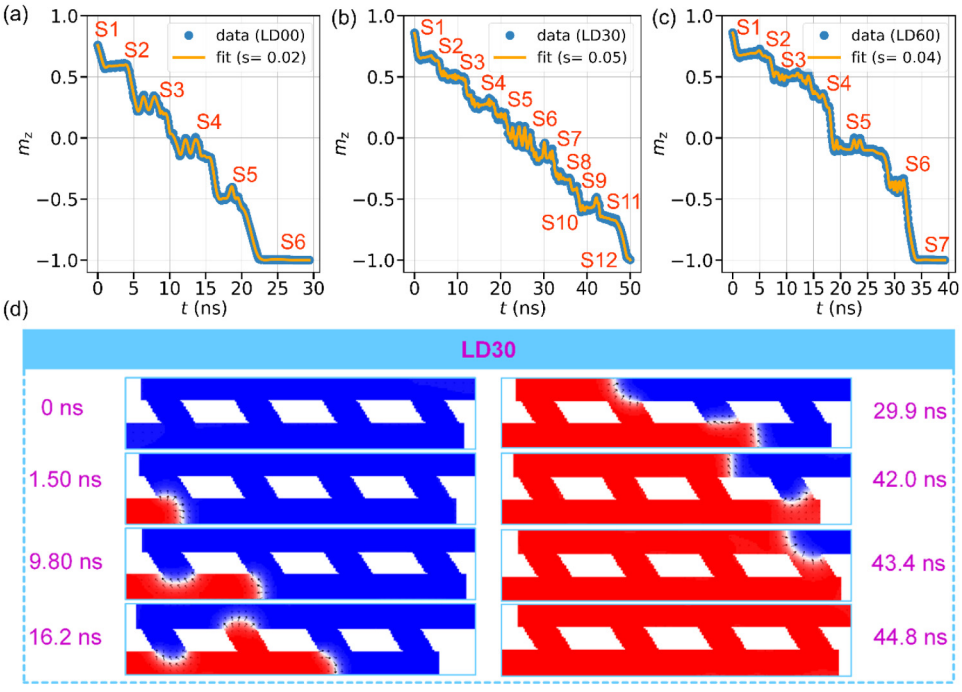

FIG. 6. The m_z vs t graph to illustrate the multilevel magnetization states in (a) LD00, (b) LD30, and (c) LD60. Here, for the smooth representation, a cubic spline was fitted to the input data points, where "s" refers the smoothing parameter.[67] (d) The simulation images of the instantaneous DW position to provide a visual understanding of DW pinning at the junctions of consecutive segments of LD30. The simulation times at which DWs attain particular configurations are mentioned beside each image.

of the magnetic domains at the pinning sites, and hence, the systematic DW motion becomes challenging. From these results, we conclude that LD30 exhibits optimized pinning strength and may be suited for experiments. We have also presented the images of instantaneous magnetization states for devices LD00 and LD60 in the supplementary material, Sec. 8.

These simulation results serve as the proof-of-concept of the pinning mechanism in the ladder device design. However, we acknowledge that for practical integration into a large-scale neuromorphic system, it is essential to implement such synaptic devices at the nanoscale-particularly within magnetic tunnel junctions (MTJs), where both the free and reference layers are structured in a ladder geometry. With such implementations, our proposed concept can evolve into a practical spintronic synapse. Nonetheless, we recognize that this would require significant optimization in terms of materials, device fabrication, and integration processes, which are beyond the scope of the current study and are being considered for future work.

Here, we also discuss the scaling effects of the proposed DW devices. As dimensions of the devices are reduced, several factors influence DW dynamics and device performance. In particular, even when the aspect ratio is maintained during geometric scaling, key parameters such as Laplace pressure (P_{Laplace}) and pinning strength are still affected. For a DW device with geometrical expansion, the depinning field is inversely proportional to the width of the nanowire.[68–70] As the width of the nanowire is reduced, the depinning field at the pinning site is expected to increase, indicating a larger P_{Laplace} and enhanced pinning strength. At nanoscale dimensions, the DW width becomes comparable to the feature size, making the system highly sensitive to edge imperfections and minor fabrication variations. These unintended defects can introduce stochastic pinning, which may compromise the reliability and repeatability of DW motion. Nevertheless, when strong geometrical pinning sites are deliberately introduced, they can dominate over such random effects and enable more controlled, reproducible behavior—although this remains a fabrication challenge. To address these issues, strategies such as high-resolution lithography, post-lithography techniques, optimized etching, and annealing process can be employed to minimize edge roughness and structural inconsistencies.[71,72]

IV. CONCLUSION

In this paper, we proposed and studied the neuron and synapse functions in uniquely designed ladder DW devices using micromagnetic simulations. In contrast to reference DW devices, our ladder DW devices with single pinning sites show the pinning of the DW for a wide range of current densities and geometric parameters. Our results show that the pinning strength of the pinning site directly depends on the geometric opening at the pinning sites. This is because P_{Laplace} on the elastic DWs is related to such an opening. In addition to DW pinning, our devices also exhibit oscillations, whose frequencies are tunable as a function of current density and magnetic parameters like saturation magnetization, anisotropy constant, and exchange constant. DW oscillations with a peak frequency of 0.25 GHz were observed, making them suitable for neuron-like behavior in neuromorphic systems. Finally, we simulated the ladder DW devices with eight pinning sites and demonstrated the multilevel magnetization states in our devices. A maximum of 12 states were observed in our devices. Moreover, a tilt of 30° provides an optimized condition for the maximum number of magnetization states. Our study provides an alternative dimension for developing DW device-based neuromorphic computing. Another exciting feature of the ladder DW device is the two-dimensional DW motion, which can be useful in spin-based logic devices.

SUPPLEMENTARY MATERIAL

See the supplementary material for more details of the simulations: Delta–Wye resistor network; DW motion in the reference wire; DW dynamics in ladder DW devices with a single pinning site, the phase diagram of ladder DW devices with a single pinning site; DW oscillations in ladder DW devices with a single pinning site; effect of material parameters on DW oscillations in ladder devices with a single pinning site; DW dynamics in full ladder DW devices with eight pinning sites; the effect of material parameters on DW oscillations in ladder devices with a single pinning site; DW dynamics in full ladder DW devices with eight pinning sites; and DW motion in full ladder DW devices: synaptic behavior.

ACKNOWLEDGMENTS

The authors acknowledge the National Research Foundation (NRF), Singapore, for the CRP21 grant (No. NRF-CRP21-2018-0003). H.R. acknowledges the Nanyang Technological University research scholarship for the financial support.

AUTHOR DECLARATIONS

Conflict of Interest

The authors have no conflicts to disclose.

Author Contributions

H.R. and D.K. contributed equally to this work.

Hasibur Rahaman: Conceptualization (equal); Data curation (equal); Formal analysis (equal); Investigation (equal); Methodology (equal); Software (equal); Validation (equal); Visualization (equal); Writing – original draft (equal); Writing – review & editing (equal). **Durgesh Kumar:** Formal analysis (equal); Methodology (equal); Writing – original draft (equal). **Ramu Maddu:** Formal analysis (equal); Writing – review & editing (equal). **Bilal Jamshed:** Formal analysis (equal). **Bipul Kumar Mahato:** Formal analysis (equal). **S. N. Piramanayagam:** Conceptualization (equal); Funding acquisition (equal); Project administration (equal); Resources (equal); Supervision (equal); Validation (equal); Writing – review & editing (equal).

DATA AVAILABILITY

The data that support the findings of this study are available from the corresponding author upon reasonable request.

REFERENCES

[1]See www.javatpoint.com for "How artificial intelligence will change the future—Javatpoint."
[2]Legal-lore, *Artificial Intelligence-future Growth and Its Implications* (Leg.-Lore, 2022).
[3]K. Hao, "The computing power needed to train AI is now rising seven times faster than ever before," in *MIT Technology Review* (MIT Technology Review, 2019), https://www.technologyreview.com/2019/11/11/132004/the-computing-power-needed-to-train-ai-is-now-rising-seven-times-faster-than-ever-before/.
[4]V. Karasenko, "Von Neumann bottlenecks in non-von Neumann Computing Architectures," Ph.D. thesis (Heidelberg University, 2020).
[5]J. Qu, "Conventional von Neumann and neuromorphic architecture of AI Chips," High. Sci. Eng. Technol. **103**, 138–143 (2024).
[6]J. Grollier, D. Querlioz, K. Camsari, K. Everschor-Sitte, S. Fukami, and M. D. Stiles, "Neuromorphic spintronics," Nat. Electron. **3**(7), 360–370 (2020).
[7]I. Chakraborty, A. Jaiswal, A. K. Saha, S. K. Gupta, and K. Roy, "Pathways to efficient neuromorphic computing with non-volatile memory technologies," Appl. Phys. Rev. **7**(2), 021308 (2020).
[8]T. Jin, W. Gan, F. Tan, N. R. Sernicola, W. S. Lew, and S. Piramanayagam, "Synaptic element for neuromorphic computing using a magnetic domain wall device with synthetic pinning sites," J. Phys. Appl. Phys. **52**(44), 445001 (2019).
[9]D. Kumar, T. Jin, S. Al Risi, R. Sbiaa, W. Lew, and S. Piramanayagam, "Domain wall motion control for racetrack memory applications," IEEE Trans. Magn. **55**(3), 1–8 (2018).
[10]D. Kuzum, S. Yu, and H.-S. Philip Wong, "Synaptic electronics: Materials, devices and applications," Nanotechnology **24**(38), 382001 (2013).
[11]J. W. Lee, J. Han, B. Kang, Y. J. Hong, S. Lee, and I. Jeon, "Strategic development of memristors for neuromorphic systems: Low-power and reconfigurable operation," Adv. Mater. **37**(19), 2413916 (2025).
[12]W. Chen, L. Song, S. Wang, Z. Zhang, G. Wang, G. Hu, and S. Gao, "Essential characteristics of memristors for neuromorphic computing," Adv. Electron. Mater. **9**(2), 2200833 (2023).
[13]T. Leonard, N. Zogbi, S. Liu, W. S. Rogers, C. H. Bennett, and J. A. C. Incorvia, "Shape anisotropy-dependent leaking in magnetic neurons for Bio-mimetic neuromorphic computing," ACS Nano **19**(3), 3470–3477 (2025).
[14]Z. Li, J. Meng, J. Yu, Y. Liu, T. Wang, P. Liu, S. Chen, H. Zhu, Q. Sun, and D. W. Zhang, "CMOS compatible low power consumption ferroelectric synapse for neuromorphic computing," IEEE Electron Device Lett. **14**, 532–535 (2023).
[15]C. D. Wright, P. Hosseini, and J. A. V. Diosdado, "Beyond von-Neumann computing with nanoscale phase-change memory devices," Adv. Funct. Mater. **23**(18), 2248–2254 (2013).
[16]D. Kumar, H. J. Chung, J. Chan, T. Jin, S. T. Lim, S. S. P. Parkin, R. Sbiaa, and S. N. Piramanayagam, "Ultralow energy domain wall device for spin-based neuromorphic computing," ACS Nano **17**(7), 6261–6274 (2023).
[17]J. Zhou and J. Chen, "Prospect of spintronics in neuromorphic computing," Adv. Electron. Mater. **7**(9), 2100465 (2021).
[18]T.-C. Hsin, C.-Y. Lin, P.-C. Wang, C. Yang, and C.-F. Pai, "All-electrical control of spin synapses for neuromorphic computing: Bridging multi-state memory with quantization for efficient neural networks," Adv. Sci. **12**(22), 2417735 (2025).
[19]Q. Shao, Z. Wang, Y. Zhou, S. Fukami, D. Querlioz, and L. O. Chua, "Spintronic memristors for computing," npj Spintron. **3**(1), 16 (2025).
[20]K. Roy, C. Wang, S. Roy, A. Raghunathan, K. Yang, and A. Sengupta, "Spintronic neural systems," Nat. Rev. Electr. Eng. **1**(11), 714–729 (2024).
[21]C. H. Marrows, J. Barker, T. A. Moore, and T. Moorsom, "Neuromorphic computing with spintronics," npj Spintron. **2**(1), 12 (2024).
[22]G. Bernard, K. Cottart, M.-A. Syskaki, V. Porée, A. Resta, A. Nicolaou, A. Durnez, S. Ono, A. M. Hernandez, J. Langer, D. Querlioz, and L. Herrera Diez, "Dynamic control of weight-update linearity in magneto-ionic synapses," Nano Lett. **25**(4), 1443–1450 (2025).
[23]X. Han, Z. Wang, Y. Wang, D. Wang, L. Zheng, L. Zhao, Q. Huang, Q. Cao, Y. Chen, L. Bai, G. Xing, Y. Tian, and S. Yan, "Neuromorphic computing in synthetic antiferromagnets by spin-orbit torque induced magnetic-field-free magnetization switching," Adv. Funct. Mater. **34**(44), 2404679 (2024).
[24]D. Ielmini, "Brain-inspired computing with resistive switching memory (RRAM): Devices, synapses and neural networks," Microelectron. Eng. **190**, 44–53 (2018).
[25]D. Kumar, T. Jin, R. Sbiaa, M. Kläui, S. Bedanta, S. Fukami, D. Ravelosona, S.-H. Yang, X. Liu, and S. Piramanayagam, "Domain wall memory: Physics, materials, and devices," Phys. Rep. **958**, 1–35 (2022).
[26]S. Dhull, W. L. W. Mah, A. Nisar, D. Kumar, H. Rahaman, B. K. Kaushik, and S. N. Piramanayagam, "Energy-efficient neural network using an anisotropy field gradient-based self-resetting neuron and meander synapse," Appl. Phys. Lett. **125**(1), 012402 (2024).
[27]D. Kumar, R. Maddu, H. J. Chung, H. Rahaman, T. Jin, S. Bhatti, S. T. Lim, R. Sbiaa, and S. N. Piramanayagam, "Emulation of neuron and synaptic functions in spin–orbit torque domain wall devices," Nanoscale Horiz. **9**(11), 1962–1977 (2024).
[28]J.-C. Jeon, A. Migliorini, J. Yoon, J. Jeong, and S. S. P. Parkin, "Multicore memristor from electrically readable nanoscopic racetracks," Science **386**(6719), 315–322 (2024).
[29]S. A. Siddiqui, S. Dutta, A. Tang, L. Liu, C. A. Ross, and M. A. Baldo, "Magnetic domain wall based synaptic and activation function generator for neuromorphic accelerators," Nano Lett. **20**(2), 1033–1040 (2020).
[30]W. L. W. Mah, D. Kumar, T. Jin, and S. Piramanayagam, "Domain wall dynamics in (Co/Ni) n nanowire with anisotropy energy gradient for neuromorphic computing applications," J. Magn. Magn. Mater. **537**, 168131 (2021).
[31]A. Brataas and K. Hals, "Spin–orbit torques in action," Nat. Nanotechnol. **9**(2), 86–88 (2014).
[32]M. Cubukcu, O. Boulle, M. Drouard, K. Garello, C. Onur Avci, I. Mihai Miron, J. Langer, B. Ocker, P. Gambardella, and G. Gaudin, "Spin-orbit torque magnetization switching of a three-terminal perpendicular magnetic tunnel junction," Appl. Phys. Lett. **104**(4), 042406 (2014).
[33]A. Sengupta and K. Roy, "Neuromorphic computing enabled by physics of electron spins: Prospects and perspectives," Appl. Phys. Express **11**(3), 030101 (2018).
[34]A. Sengupta, S. H. Choday, Y. Kim, and K. Roy, "Spin orbit torque based electronic neuron," Appl. Phys. Lett. **106**(14), 143701 (2015).
[35]L. Liu, D. Wang, D. Wang, Y. Sun, H. Lin, X. Gong, Y. Zhang, R. Tang, Z. Mai, Z. Hou, Y. Yang, P. Li, L. Wang, Q. Luo, L. Li, G. Xing, and M. Liu, "Domain wall magnetic tunnel junction-based artificial synapses and neurons for all-spin neuromorphic hardware," Nat. Commun. **15**(1), 4534 (2024).
[36]T. Ono, H. Miyajima, K. Shigeto, and T. Shinjo, "Magnetization reversal in submicron magnetic wire studied by using giant magnetoresistance effect," Appl. Phys. Lett. **72**(9), 1116–1117 (1998).
[37]M. Kläui, C. Vaz, J. Bland, W. Wernsdorfer, G. Faini, and E. Cambril, "Domain wall pinning and controlled magnetic switching in narrow ferromagnetic ring structures with notches," J. Appl. Phys. **93**(10), 7885–7890 (2003).
[38]M. Hayashi, L. Thomas, C. Rettner, R. Moriya, X. Jiang, and S. S. P. Parkin, "Dependence of current and field driven depinning of domain walls on their structure and chirality in permalloy nanowires," Phys. Rev. Lett **97**(20), 207205 (2006).
[39]S. S. Parkin, M. Hayashi, and L. Thomas, "Magnetic domain-wall racetrack memory," Science **320**(5873), 190–194 (2008).
[40]M. Al Bahri, B. Borie, T. Jin, R. Sbiaa, M. Kläui, and S. Piramanayagam, "Staggered magnetic nanowire devices for effective domain-wall pinning in racetrack memory," Phys. Rev. Appl. **11**(2), 024023 (2019).
[41]H. Rahaman, D. Kumar, H. J. Chung, R. Maddu, S. T. Lim, T. Jin, and S. N. Piramanayagam, "Diode characteristics in magnetic domain wall devices via geometrical pinning for neuromorphic computing," ACS Appl. Mater. Interfaces **15**, 15832–15838 (2023).

[42]I. Polenciuc, A. J. Vick, D. A. Allwood, T. J. Hayward, G. Vallejo-Fernandez, K. O'Grady, and A. Hirohata, "Domain wall pinning for racetrack memory using exchange bias," Appl. Phys. Lett. **105**(16), 162406 (2014).
[43]T. Jin, D. Kumar, W. Gan, M. Ranjbar, F. Luo, R. Sbiaa, X. Liu, W. S. Lew, and S. Piramanayagam, "Nanoscale compositional modification in Co/Pd multilayers for controllable domain wall pinning in racetrack memory," Phys. Status Solidi RRL **12**(10), 1800197 (2018).
[44]C. A. Durner, A. Migliorini, J.-C. Jeon, and S. S. P. Parkin, "Reconfigurable magnetic inhibitor for domain wall logic and neuronal devices," ACS Nano **19**(5), 5316–5325 (2025).
[45]T. Lee, S. Jeong, S. Kim, and K.-J. Kim, "Position-reconfigurable pinning for magnetic domain wall motion," Sci. Rep. **13**(1), 6791 (2023).
[46]X. Chen, W. Liu, and M. T. Bryan, "Dipolar field-assisted domain wall depinning in trilayer structures," IEEE Trans. Magn. (2025), available at https://resourcecenter.magnetics.ieee.org/conferences/joint-2025/mags_conf_joint_2025_0048.
[47]D. Kumar, J. Chan, and S. Piramanayagam, "Domain wall pinning through nanoscale interfacial Dzyaloshinskii–Moriya interaction," J. Appl. Phys. **130**(21), 213901 (2021).
[48]R. Sbiaa, M. A. Bahri, and S. N. Piramanayagam, "Domain wall oscillation in magnetic nanowire with a geometrically confined region," J. Magn. Magn. Mater. **456**, 324–328 (2018).
[49]M. Voto, L. Lopez-Diaz, and E. Martinez, "Pinned domain wall oscillator as a tuneable direct current spin wave emitter," Sci. Rep. **7**(1), 13559 (2017).
[50]A. Vansteenkiste, J. Leliaert, M. Dvornik, M. Helsen, F. Garcia-Sanchez, and B. Van Waeyenberge, "The design and verification of MuMax3," AIP Adv. **4**(10), 107133 (2014).
[51]J. M. Lee, K. Cai, G. Yang, Y. Liu, R. Ramaswamy, P. He, and H. Yang, "Field-free spin–orbit torque switching from geometrical domain-wall pinning," Nano Lett. **18**(8), 4669–4674 (2018).
[52]J. J. Joos, P. Bassirian, P. Gypens, J. Mulkers, K. Litzius, B. Van Waeyenberge, and J. Leliaert, "Tutorial: Simulating modern magnetic material systems in mumax3," J. Appl. Phys. **134**(17), 171101 (2023).
[53]Y. Liu, T. Yu, Z. Zhu, H. Zhong, K. M. Khamis, and K. Zhu, "High thermal stability in W/MgO/CoFeB/W/CoFeB/W stacks via ultrathin W insertion with perpendicular magnetic anisotropy," J. Magn. Magn. Mater. **410**, 123–127 (2016).
[54]K.-U. Demasius, T. Phung, W. Zhang, B. P. Hughes, S.-H. Yang, A. Kellock, W. Han, A. Pushp, and S. S. P. Parkin, "Enhanced spin-orbit torques by oxygen incorporation in tungsten films," Nat. Commun. **7**(1), 10644 (2016).
[55]Electrical World and Engineer, Inc., *Electrical World and Engineer* (McGraw Hill Publications Company, 1899), Vol. 34, Issue 12; available at https://archive.org/details/sim_electrical-world_1899-09-16_34_12/mode/2up.
[56]W. Döring, "Über die Trägheit der Wände zwischen Weißschen Bezirken," Z. Naturforsch. A **3**(7), 373–379 (1948).
[57]Z.-D. Li, X.-M. Nan, and W. M. Liu, "Magnetization spiral structure and high domain wall velocity induced by inertial effect," Physica E **159**, 115931 (2024).
[58]T. H. O'Dell, "Domain wall mass in magnetic bubble films under large in-plane fields," Phys. Status Solidi A **54**(1), 429–436 (1979).
[59]I. Rissanen and L. Laurson, "Magnetic non-contact friction from domain wall dynamics actuated by oscillatory mechanical motion," J. Phys. Appl. Phys. **52**(44), 445002 (2019).
[60]A. Slavin and V. Tiberkevich, "Nonlinear auto-oscillator theory of microwave generation by spin-polarized current," IEEE Trans. Magn. **45**(4), 1875–1918 (2009).
[61]E. R. J. Edwards, H. Ulrichs, V. E. Demidov, S. O. Demokritov, and S. Urazhdin, "Parametric excitation of magnetization oscillations controlled by pure spin current," Phys. Rev. B **86**(13), 134420 (2012).
[62]J. Qiu, P. Chen, M. Wang, D. Yang, J. Cao, M. Liu, J. Yu, X. Zhang, H. Cheng, Q. Liu, and M. Liu, "Compact artificial synapse-neuron module with chemically mediated spiking behaviors," ACS Nano **19**(12), 12298–12307 (2025).
[63]S. H. Sung, T. J. Kim, H. Shin, T. H. Im, and K. J. Lee, "Simultaneous emulation of synaptic and intrinsic plasticity using a memristive synapse," Nat. Commun. **13**(1), 2811 (2022).
[64]X. Zhang, N. Vernier, W. Zhao, H. Yu, L. Vila, Y. Zhang, and D. Ravelosona, "Direct observation of domain-wall surface tension by deflating or inflating a magnetic bubble," Phys. Rev. Appl. **9**(2), 024032 (2018).
[65]Y. Zhang, X. Zhang, N. Vernier, Z. Zhang, G. Agnus, J.-R. Coudevylle, X. Lin, Y. Zhang, Y.-G. Zhang, and W. Zhao, "Domain-wall motion driven by Laplace pressure in Co−Fe−B/MgO nanodots with perpendicular anisotropy," Phys. Rev. Appl. **9**(6), 064027 (2018).
[66]A. Thiaville, S. Rohart, É. Jué, V. Cros, and A. Fert, "Dynamics of Dzyaloshinskii domain walls in ultrathin magnetic films," Europhys. Lett. **100**(5), 57002 (2012).
[67]C. de Boor, "Review of a practical guide to splines.," Math. Comput. **34**(149), 325–326 (1980).
[68]M. Ramu, S. Goolaup, W. L. Gan, S. Krishnia, G. J. Lim, and W. S. Lew, "Spin orbit torque induced asymmetric depinning of chiral Néel domain wall in Co/Ni heterostructures," Appl. Phys. Lett. **110**(16), 162402 (2017).
[69]J. Wunderlich, D. Ravelosona, C. Chappert, F. Cayssol, V. Mathet, J. Ferre, J.-P. Jamet, and A. Thiaville, "Influence of geometry on domain wall propagation in a mesoscopic wire," IEEE Trans. Magn. **37**(4), 2104–2107 (2001).
[70]K.-J. Kim, G.-H. Gim, J.-C. Lee, S.-M. Ahn, K.-S. Lee, Y. J. Cho, C.-W. Lee, S. Seo, K.-H. Shin, and S.-B. Choe, "Depinning field at notches of ferromagnetic nanowires with perpendicular magnetic anisotropy," IEEE Trans. Magn. **45**(10), 4056–4058 (2009).
[71]Z. Yu, L. Chen, W. Wu, H. Ge, and S. Y. Chou, "Fabrication of nanoscale gratings with reduced line edge roughness using nanoimprint lithography," J. Vac. Sci. Technol. B **21**(5), 2089–2092 (2003).
[72]M. Guo, Z. Qu, F. Min, Z. Li, Y. Qiao, and Y. Song, "Advanced unconventional techniques for sub-100 nm nanopatterning," InfoMat **4**(8), e12323 (2022).